Received: 1 November 2021 | Revised: 27 November 2021 | Accepted: 15 December 2021

DOI: 10.1111/ffe.13638

SPECIAL ISSUE ARTICLE

FFEMS Fatigue & Fracture of Engineering Materials & Structures WILEY

Modelling fatigue crack growth in shape memory alloys

Marlini Simoes[1,2] | **Christopher Braithwaite**[1] | **Advenit Makaya**[2] | **Emilio Martínez-Pañeda**[3]

[1]Cavendish Laboratory, University of Cambridge, Cambridge, UK

[2]ESA-ESTEC, Noordwijk, The Netherlands

[3]Department of Civil and Environmental Engineering, Imperial College London, London, UK

Correspondence Emilio Martínez-Pañeda, Department of Civil and Environmental Engineering, Imperial College London, London SW7 2AZ, UK.
Email: e.martinez-paneda@imperial.ac.uk

Funding information
Engineering and Physical Sciences Research Council, Grant/Award Number: EP/R512461/1; European Space Agency, Grant/Award Number: 4000125861; UK Research and Innovation, Grant/Award Number: MR/V024124/1

Abstract

We present a phase field-based framework for modelling fatigue damage in Shape Memory Alloys (SMAs). The model combines, for the first time: (i) a generalized phase field description of fracture, incorporating multiple phase field formulations, (ii) a constitutive model for SMAs, based on a Drucker–Prager form of the transformation surface, and (iii) a fatigue degradation function, with damage driven by both elastic and transformation strains. The theoretical framework is numerically implemented, and the resulting linearized system is solved using a robust monolithic scheme, based on quasi-Newton methods. Several paradigmatic boundary value problems are addressed to gain insight into the role of transformation stresses, stress-strain hysteresis, and temperature. Namely, we compute $\Delta\varepsilon - N$ curves, quantify Paris law parameters, and predict fatigue crack growth rates in several geometries. In addition, the potential of the model for solving large-scale problems is demonstrated by simulating the fatigue failure of a 3D lattice structure.

KEYWORDS

fatigue, finite element analysis, fracture, phase field, shape memory alloys

1 | INTRODUCTION

Shape Memory Alloys (SMAs) have received significant attention due to their remarkable properties.[1] Owing to their capacity to undergo a thermal and/or stress-induced solid-to-solid phase transformation, SMAs exhibit the largest reversible strains of all crystalline materials - of up to 10%, one order of magnitude higher than traditional alloys. The ability of SMAs to recover their original shape and display a recoverable nonlinear response under very large strains has fostered their application in a wide range of sectors, from biomedical devices to aerospace components.[2,3] In many of these applications, structural integrity is paramount. Experiments and theoretical modelling have shown that there is a toughening effect associated with phase transformation.[4-6] Transformation strains resulting from the phase change provide a source of energy dissipation that enhances crack growth resistance.[7,8] The yield stress of SMAs is typically much larger than the threshold for stress-induced transformation, and as a result, a transformation zone develops in the vicinity of the crack tip. As shown in Figure 1 for the case of a NiTi alloy (arguably the most widely exploited class of SMAs), the distribution of crack tip stresses shows three regions: (1) an outer austenitic region ($\xi = 0$), (2) an intermediate austenite–martensite transformation region ($0 < \xi < 1$), and (3) an inner martensitic region ($\xi = 1$).[8,9] These features govern the fracture and fatigue response of SMAs.[10-12]

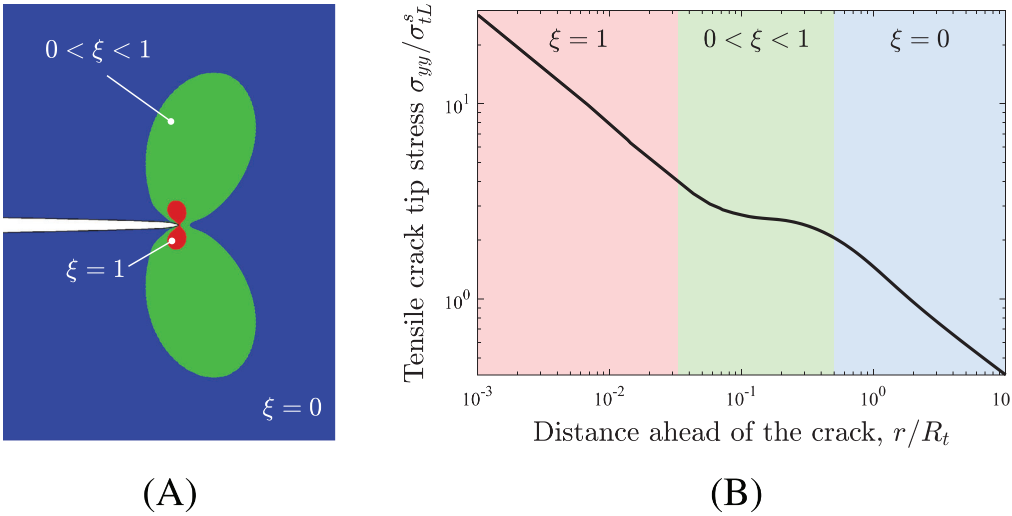

FIGURE 1 Crack tip mechanics of SMAs under small scale transformation zone conditions: (A) crack tip contours, and (B) tensile stress distribution ahead of the crack, in a log–log plot. Three regions are differentiated, based on the magnitude of the martensitic volume fraction ξ. The tensile stress distribution is normalized by the transformation stress threshold σ_{tL}^s, and the distance ahead of the crack r is normalized by an Irwin-like estimation of the transformation zone length: $R_t = (1/3\pi)(K_I/\sigma_{tL}^s)^2$, where K_I is the stress intensity factor [Colour figure can be viewed at wileyonlinelibrary.com]

The fatigue behavior of SMAs has been the focus of much attention as the most successful applications of SMAs involve significant cyclic mechanical motion; for example, actuator springs or medical devices such as stents.[13-18] However, the vast majority of the literature in the area of SMA fatigue is experimental, and there is a need for modelling endeavors that can provide further insight, optimize design, and map safe regimes of operation. While efforts have been made to model the constitutive behavior of SMAs under cyclic loading,[19-21] and to quantify the stationary stress fields ahead of cracks and notches,[22,23] the study of subcritical crack growth remains an elusive goal. This is despite its importance for defect-tolerant design approaches. Very recently, Simoes and Martínez-Pañeda[8] presented a phase field formulation for modelling crack growth in SMAs. They formulated a generalized phase field theory and combined it with the unified SMA model by Lagoudas et al.[24] Phase field models can readily capture cracking phenomena of arbitrary complexity and have been recently extended to fatigue damage (see, e.g., previous studies[25-28] and Refs. therein).

In this work, we develop a new model for fatigue crack growth in SMAs. The constitutive SMA model by Auricchio and Taylor[29] is combined with a phase field formulation for fracture and fatigue, where the damage driving force involves both elastic and transformation strains. The model is general and aims at capturing a wide range of material behavior, thus accommodating both `AT1`[30] and `AT2`[31] phase field theories. Numerical robustness and efficiency are achieved by using a quasi-Newton-based monolithic solution scheme.[32,33] Several paradigmatic boundary value problems are investigated to gain insight into the fatigue response of SMAs. Firstly, we produce *Virtual* $\Delta\varepsilon - N$ curves and assess the influence of temperature and stress-strain hysteresis. Secondly, crack extension is predicted in a single-edged notched tension specimen considering different definitions of the crack density function. Thirdly, we obtain da/dN versus ΔK curves and predict the associated Paris law parameters for different material modelling choices. Finally, we investigate the evolution of fatigue cracks in a 3D SMA lattice structure undergoing cyclic loading.

The remainder of this manuscript is organized as follows. In Section 2, we present the theoretical framework for our phase field fatigue SMA model. Details of the numerical implementation are provided in Section 3. Section 4 is dedicated to showcasing the predictions of the model and discussing the interpretation of the finite element results presented in the context of the literature. Finally, concluding remarks are given in Section 5.

2 | A PHASE FIELD FATIGUE FORMULATION FOR SMAs

Here, the theory underlying our phase field-based model for fatigue in SMAs is presented. First, in Section 2.1, we describe the phase field regularization of fracture. Then, in Section 2.2, the extension to fatigue and the variational formulation are presented. Finally, Section 2.3 provides a brief outline of the constitutive model employed to capture the mechanical response of SMAs. For simplicity, small strains and isothermal behavior are assumed; we will assess the influence of temperature by conducting numerical experiments at different temperatures but disregard thermal loads. Plastic deformations are also considered a secondary effect and neglected for simplicity, as the yield stress of SMAs is typically much larger than the transformation stress.

2.1 | A phase field description of fracture

Phase field methods have become very popular in the modelling of a wide range of interfacial problems, from microstructural evolution[34] to corrosion.[35] By using an auxiliary variable, the phase field ϕ, a given interface can be smeared over the computational domain. The interface is no longer sharp and of zero thickness, but smooth and of a finite thickness, as governed by a length scale parameter. This paradigm greatly facilitates the computational treatment of evolving interfaces, as the interface equation is defined in the entire domain (i.e., no special treatment is needed) and topological changes such as divisions or merging of interfaces are naturally captured. In fracture mechanics, the phase field describes the location of the crack (solid-crack interface), taking (e.g.) a value of $\phi = 0$ in intact material points and of $\phi = 1$ in fully cracked material points, and varying smoothly in-between (akin to a damage variable). Phase field fracture methods have opened new modelling horizons, enabling the prediction of complex cracking phenomena such as crack branching, deflection, nucleation, and merging in arbitrary geometries and dimensions.[36-39] Applications have soared and now include the fracture of functionally graded materials,[40,41] composites,[42-44] rock-like materials,[45,46] ductile[47-49] and embrittled[50-52] metals, and natural materials.[53,54] The evolution of the phase field ϕ is generally defined based on Griffith's[55] energy balance and the thermodynamics of fracture.[31,56] Thus, crack growth is driven by the competition between the energy released by the solid and the energy required to create two new surfaces, often referred to as G_c, the critical energy release rate or the material toughness. Accordingly, the diffuse phase field representation introduces the following approximation of the fracture energy over a discontinuous surface Γ:

$$\Phi = \int_\Gamma G_c \, \mathrm{d}S \approx \int_\Omega G_c \left[\frac{1}{4 c_w \ell} \left(w(\phi) + \ell^2 |\nabla \phi|^2 \right) \right] \mathrm{d}V, \quad (1)$$

for $\ell \to 0^+$.

Here, ℓ is the phase field length scale, $w(\phi)$ is the geometric crack function, and c_w is a scaling constant, defined as $c_w = \int_0^1 \sqrt{w(\zeta)} \mathrm{d}\zeta$. The choice of $w(\phi)$ defines the damage constitutive behavior. In this work, we aim at providing a generalized framework by incorporating both the so-called `AT1`[30] and `AT2`[31] phase field models. The `AT2` formulation is recovered for $w(\phi) = \phi^2$ $(c_w = 1/2)$ while in the `AT1` model, $w(\phi) = \phi$ $(c_w = 2/3)$. Thus, the main difference between the `AT1` and the `AT2` models is that the latter does not have a damage threshold (as $w'(0) = 0$), while the `AT1` formulation exhibits a linear elastic regime prior to the onset of damage.

It has been recently emphasized that for a finite value of ℓ, variational phase field fracture models exhibit a finite strength, which enables capturing the crack size effect.[57,58] The critical failure stress and the critical failure strain can be related to the elastic and fracture properties by solving the homogeneous 1D problem ($\nabla \phi = 0$), giving[57]

$$\texttt{AT1}: \sigma_c = \sqrt{\frac{3 E G_c}{8 \ell}}, \quad \varepsilon_c = \sqrt{\frac{3 G_c}{8 \ell E}}. \quad (2)$$

$$\texttt{AT2}: \sigma_c = \sqrt{\frac{27 E G_c}{256 \ell}}, \quad \varepsilon_c = \sqrt{\frac{G_c}{3 \ell E}}. \quad (3)$$

2.2 | Variational phase field fatigue

Let us now formulate the variational problem, incorporating both bulk $\boldsymbol{\Psi}^b$ and surface $\boldsymbol{\Psi}^s$ energies, and introduce fatigue damage into the formulation. The latter is achieved by defining a fatigue degradation function $f(\overline{\alpha})$, where $\overline{\alpha}$ is a cumulative history variable. Accordingly, the total potential energy is given by:

$$\begin{aligned} \boldsymbol{\Psi} &= \boldsymbol{\Psi}^b(\boldsymbol{\varepsilon}, \xi, \phi) + \boldsymbol{\Psi}^s(\phi, \overline{\alpha}) \\ &= \int_\Omega \left\{ (1-\phi)^2 \psi(\boldsymbol{\varepsilon}, \xi) + f(\overline{\alpha}) \frac{G_c}{4 c_w \ell} \left(w(\phi) + \ell^2 |\nabla \phi|^2 \right) \right\} \mathrm{d}V, \end{aligned} \quad (4)$$

where ψ is the strain energy density and $\boldsymbol{\varepsilon}$ is the strain tensor. Both can be divided into their elastic and transformation parts, such that the total strain energy density ψ is given by

$$\psi(\boldsymbol{\varepsilon}, \xi) = \int_0^t (\boldsymbol{\sigma} : \dot{\boldsymbol{\varepsilon}}^e) \mathrm{d}t + \int_0^t (\boldsymbol{\sigma} : \dot{\boldsymbol{\varepsilon}}^t) \mathrm{d}t, \quad (5)$$

where $\boldsymbol{\varepsilon}^e$ and $\boldsymbol{\varepsilon}^t$, respectively denote the elastic and transformation strain tensors. Since the fracture driving force is the total strain energy density, both elastic and transformation strains are assumed to contribute to material damage.

We proceed now to define the fatigue degradation function $f(\overline{\alpha})$. Here, we follow the work by Carrara et al.[25] and adopt the following asymptotic function:

$$f(\overline{\alpha}(t)) = \begin{cases} 1 & \text{if} \, \overline{\alpha}(t) \leq \alpha_T \\ \left(\frac{2\alpha_T}{\overline{\alpha}(t)+\alpha_T}\right)^2 & \text{if} \, \overline{\alpha}(t) \geq \alpha_T \end{cases}, \tag{6}$$

where α_T is a fatigue threshold parameter, defined as $\alpha_T = G_c/(12\ell)$.[25] The fatigue history variable $\overline{\alpha}$ is computed as,

$$\overline{\alpha}(t) = \int_0^t H(\alpha\dot{\alpha})|\dot{\alpha}|\,\mathrm{d}t, \tag{7}$$

where $H(\alpha\dot{\alpha})$ is the Heaviside function, introduced to ensure that $\overline{\alpha}$ only increases during loading. Finally, consistent with our definition of the fracture driving force, the fatigue history variable is defined as

$$\alpha = (1-\phi)^2\psi. \tag{8}$$

2.3 | Constitutive behavior of SMAs

The constitutive response of the phase transforming solid is based on the material model for SMAs developed Auricchio and coworkers.[29,59] Accordingly, the elastic properties (Young's modulus E and Poisson's ratio ν) are derived using the rule of mixtures from the corresponding austenitic and martensitic properties, where ξ is the volume fraction of martensite; that is,

$$E = E_A + \xi(E_M - E_A), \tag{9}$$

$$\nu = \nu_A + \xi(\nu_M - \nu_A). \tag{10}$$

The evolution of the transformation strains is estimated using a Drucker–Prager type of loading function. The increment in transformation strain is given by the following flow rule:

$$\Delta\boldsymbol{\varepsilon}^t = \Delta\xi\frac{\partial G^t}{\partial\boldsymbol{\sigma}}. \tag{11}$$

where G^t is the transformation flow potential. Both G^t and the transformation surface F^t are assumed to follow a Drucker–Prager form:

$$G^t = \sqrt{\frac{3}{2}\boldsymbol{\sigma}':\boldsymbol{\sigma}'} + \frac{1}{3}\mathrm{tr}\,(\boldsymbol{\sigma})\tan\varphi. \tag{12}$$

$$F^t = \sqrt{\frac{3}{2}\boldsymbol{\sigma}':\boldsymbol{\sigma}'} + \frac{1}{3}\mathrm{tr}\,(\boldsymbol{\sigma})\tan\beta. \tag{13}$$

Here, the angles φ and β are material constants estimated from the tensile and compressive transformation stress levels, the uniaxial transformation strain, and the volumetric transformation strain.[29] This ensures that the pressure dependency of phase transformations is captured. We emphasize that other constitutive SMA choices can be coupled with the phase field fatigue descriptions of fracture and fatigue presented in Sections 2.1 and 2.2, respectively.

3 | NUMERICAL IMPLEMENTATION

Details of the numerical implementation are provided here, starting with the enforcement of damage irreversibility (Section 3.1), followed by the finite element discretization and formulation of the residuals and stiffness matrices (Section 3.2), the quasi-Newton solution scheme employed (Section 3.3), and the particularities of the implementation in the commercial finite element package `ABAQUS` through a user-defined `UELMAT` subroutine (Section 3.4).

3.1 | Damage irreversibility

A history variable field $\mathcal{H}$ is introduced to ensure damage irreversibility, $\phi_{n+1} \geq \phi_n$. Thus, the history field must satisfy the Kuhn–Tucker conditions

$$\psi - \mathcal{H} \leq 0, \qquad \dot{\mathcal{H}} \geq 0, \qquad \dot{\mathcal{H}}(\psi - \mathcal{H}) = 0. \tag{14}$$

Accordingly, for a current time t, the history field can be defined as

$$\mathcal{H} = \max_{\tau \in [0,t]} \psi(\tau). \tag{15}$$

Also, one should note that the `AT1` phase field formulation does not inherently ensure that the lower bound on the phase field is enforced. If no measures are taken, the phase field can become negative for strains below the critical one, ε_c, Equation (2). To prevent this, we define the following threshold value for the history field:

$$\mathcal{H}^{\mathtt{AT1}}_{min} = \frac{3G_c}{16\ell}. \tag{16}$$

3.2 | Finite element discretization

We shall now formulate the two-field weak form and subsequently derive the stiffness matrices and residuals applying a finite element discretization. Thus, consider the total potential energy of the solid, Equation (4). In the absence of body forces and external tractions, the first variation of (4) with respect to $\boldsymbol{\varepsilon}$ and ϕ, gives

$$\int_\Omega \left[(1-\phi)^2 \boldsymbol{\sigma} : \delta\boldsymbol{\varepsilon}\right] \mathrm{d}V = 0, \tag{17}$$

$$\int_\Omega \left[-2(1-\phi)\delta\phi\mathcal{H} + f(\overline{\alpha})G_c\left(\frac{\phi}{\ell}\delta\phi + \ell\nabla\phi\cdot\nabla\delta\phi\right)\right]\mathrm{d}V = 0, \tag{18}$$

where we have made use of the history field concept. Now, adopting Voigt notation, consider the following finite element interpolation for the nodal variables: the displacement vector $\mathbf{u}$ and the phase field ϕ,

$$\mathbf{u} = \sum_{i=1}^{m} \boldsymbol{N}_i^{\mathbf{u}}\mathbf{u}_i \quad \text{and} \quad \phi = \sum_{i=1}^{m} N_i\phi_i, \tag{19}$$

where n is the number of nodes and $\boldsymbol{N}_i$ denotes the shape function matrix, a diagonal matrix with N_i in the diagonal terms. Consequently, the corresponding derivatives can be discretized making use of the strain-displacement matrices $\boldsymbol{B}_i^{\mathbf{u}}$ and $\boldsymbol{B}_i^{\phi}$ as follows:

$$\boldsymbol{\varepsilon} = \sum_{i=1}^{m} \boldsymbol{B}_i^{\mathbf{u}}\mathbf{u}_i \quad \text{and} \quad \nabla\phi = \sum_{i=1}^{m} \boldsymbol{B}_i^{\phi}\phi_i. \tag{20}$$

Making use of this discretization and considering that (17) and (18) must hold for arbitrary values of the primal kinematic variables, the residuals are derived as

$$\boldsymbol{r}_i^{\mathbf{u}} = \int_\Omega \left\{\left[(1-\phi)^2 + \kappa\right]\left(\boldsymbol{B}_i^{\mathbf{u}}\right)^T \boldsymbol{\sigma}\right\}\mathrm{d}V, \tag{21}$$

$$r_i^{\phi} = \int_\Omega \left\{-2(1-\phi)N_i\mathcal{H} + \frac{G_c}{2c_w\ell}\left[\frac{w'(\phi)}{2}N_i + \ell^2\left(\boldsymbol{B}_i^{\phi}\right)^T\nabla\phi\right]\right\}\mathrm{d}V, \tag{22}$$

where κ is a small positive constant introduced to keep the system of equations well-conditioned. As commonly done in the literature (see, e.g., Martínez-Pañeda et al.[52]), a value of $\kappa = 1\times10^{-7}$ is adopted throughout this manuscript. Finally, the tangent stiffness matrices are derived as:

$$\boldsymbol{K}_{ij}^{\mathbf{uu}} = \frac{\partial \boldsymbol{r}_i^{\mathbf{u}}}{\partial \mathbf{u}_j} = \int_\Omega \left\{\left[(1-\phi)^2 + \kappa\right]\left(\boldsymbol{B}_i^{\mathbf{u}}\right)^T \boldsymbol{\mathcal{C}}\boldsymbol{B}_j^{\mathbf{u}}\right\}\mathrm{d}V, \tag{23}$$

$$\boldsymbol{K}_{ij}^{\phi\phi} = \frac{\partial r_i^{\phi}}{\partial \phi_j} = \int_\Omega \left\{\left(2\mathcal{H} + \frac{G_c}{4c_w\ell}w''(\phi)\right)N_iN_j + \frac{G_c\ell}{2c_w}\left(\boldsymbol{B}_i^{\phi}\right)^T\left(\boldsymbol{B}_j^{\phi}\right)\right\}\mathrm{d}V, \tag{24}$$

where $\boldsymbol{\mathcal{C}}$ is the material Jacobian.

3.3 | Solution scheme

The resulting system of equations is solved in a monolithic manner, using a quasi-Newton approach, which requires the stiffness matrix to be symmetric and positive-definite. Accordingly, the non-diagonal terms of the stiffness matrix are taken to be equal to zero and the resulting system reads:

$$\begin{Bmatrix} \mathbf{u} \\ \boldsymbol{\phi} \end{Bmatrix}_{t+\Delta t} = \begin{Bmatrix} \mathbf{u} \\ \boldsymbol{\phi} \end{Bmatrix}_{t} - \begin{bmatrix} \mathbf{K}^{\mathbf{uu}} & 0 \\ 0 & \mathbf{K}^{\phi\phi} \end{bmatrix}_t^{-1} \begin{Bmatrix} \mathbf{r}^{\mathbf{u}} \\ \mathbf{r}^{\phi} \end{Bmatrix}_t. \tag{25}$$

A global iterative scheme is adopted to obtain the solutions for which $\boldsymbol{r}^{\mathbf{u}} = \boldsymbol{0}$ and $\mathbf{r}^{\phi} = \boldsymbol{0}$. The total potential energy functional is non-convex with respect to $\mathbf{u}$ and ϕ, but quasi-Newton methods have shown to be very robust when dealing with non-convex minimization problems.[32,33] Specifically, the so-called Broyden–Fletcher–Goldfarb–Shanno (BFGS) algorithm is used.[60] Thus, if the linearized system is described as:

$$\tilde{\mathbf{K}}\Delta\mathbf{z} = \Delta\mathbf{r} \quad \text{with} \quad \mathbf{z} = \begin{Bmatrix} \mathbf{u} \\ \boldsymbol{\phi} \end{Bmatrix}, \tag{26}$$

then the approximated stiffness matrix is defined as follows:

$$\tilde{\mathbf{K}} = \tilde{\mathbf{K}}_t - \frac{\left(\tilde{\mathbf{K}}_t\Delta\mathbf{z}\right)\left(\tilde{\mathbf{K}}_t\right)\Delta\mathbf{z}\Big)^T}{\Delta\mathbf{z}\tilde{\mathbf{K}}_t\Delta\mathbf{z}} + \frac{\Delta\mathbf{r}\Delta\mathbf{r}^T}{\Delta\mathbf{z}^T\Delta\mathbf{r}}. \tag{27}$$

Since the SMA constitutive model is implemented using an implicit integration scheme, unconditional stability is guaranteed, speeding up calculations by several orders of magnitude relative to staggered solution schemes.[32]

3.4 | Details of the `ABAQUS` implementation

A `UELMAT` subroutine is developed to implement the theory described in Section 2 into the commercial finite element package `ABAQUS`. The `UELMAT`, like a user element (`UEL`) subroutine, requires defining the element residual and stiffness matrices; `ABAQUS` is used only to assemble the global matrices and solve the system. However, the `UELMAT` differs from the `UEL` in that it provides access to `ABAQUS`'s material library (`material_lib_mech`). We exploit this to obtain the stress tensor $\boldsymbol{\sigma}$ and the SMA material Jacobian $\boldsymbol{\mathcal{C}}$ for a given strain tensor. Abaqus2Matlab[61] is used to pre-process the input files. The code developed can be downloaded from https://www.empaneda.com/codes.

4 | RESULTS

The computational framework presented in Sections 2 and 3 is used to gain insight into the fatigue behavior of SMAs. To investigate the role of temperature and of the size of the stress-strain hysteresis, we conduct our numerical experiments considering three different scenarios from the point of view of SMA deformation behaviour; these are labeled C1, C2, and C3. The case C1 involves a reference material, which is determined by fitting the uniaxial stress-strain response of an equiatomic NiTi SMA, as measured by Strandel et al.[62] - see Figure 2A. Four regions can be readily identified. First, the response is linear elastic and governed by the elastic constants of the austenite phase (E_A, ν_A). Eventually, the stress reaches the threshold transformation stress for loading, σ_{tL}^{s}, and transformation to the martensite phase begins. The transformation process ends when the final transformation stress σ_{tL}^{f} is reached. Upon further loading, the material behavior is elastic but governed by the martensite elastic properties (E_M, ν_M). If the load is removed, a martensite to austenite phase transformation will begin when the stress reaches the unloading threshold, σ_{tU}^{s}. The material will be fully austenitic when the final stress for transformation under unloading is attained, σ_{tU}^{f}. The values reported in Table 1 provided the best fit to the experimental data by Strandel et al.[62] and are used throughout this paper unless otherwise stated. As in the experiments, numerical results for the reference material, C1, are obtained adopting a testing temperature of $T = 320\,\mathrm{K}$. It is worth noting that, while the model seems to provide a good approximation to the uniaxial experiments by Strandel et al.[62] (Figure 2A), a better agreement can be obtained by incorporating additional modelling features. For example, the unified model of Lagoudas[1] includes additional smooth hardening parameters that enable following more closely the transformation regions. Also, the residual strain seen in the experiments after unloading can be readily captured by considering plastic deformation.

The experimental literature reports a significant influence of the testing temperature and of the size of the stress-strain hysteresis (see, e.g., Wilkes and Liaw[12] and Refs. therein). To investigate the latter, we adopt the material parameters of Table 1 but vary by 10% the transformation stress thresholds, in what we refer to as case study C2. Specifically, we make the hysteresis loop smaller by reducing by 10% the loading stress thresholds, such that $\sigma_{tL}^{s} = 410.85\,\mathrm{MPa}$ and $\sigma_{tL}^{f} = 507.38\,\mathrm{MPa}$, and by increasing by 10% the unloading stress thresholds, rendering $\sigma_{tU}^{s} = 399.3\,\mathrm{MPa}$ and $\sigma_{tU}^{f} = 229.9\,\mathrm{MPa}$. To quantify the role of temperature, we use the material properties

TABLE 1 Material parameters used for the reference material, following the calibration with the uniaxial stress-strain measurements by Strnadel et al.[62] on an equiatomic nitinol SMA

Parameter	Magnitude
Austenite's Young's modulus, E_A (MPa)	41,000.0
Martensite's Young's modulus, E_M (MPa)	22,000.0
Austenite's Poisson's ratio, ν_A	0.33
Martensite's Poisson's ratio, ν_M	33.0
Transformation strain, ε_L	0.0335
Start of transformation stress (loading), σ_{tL}^{s} (MPa)	456.5
End of transformation stress (loading), σ_{tL}^{f} (MPa)	563.8
Start of transformation stress (unloading), σ_{tU}^{s} (MPa)	363.0
End of transformation stress (unloading), σ_{tU}^{f} (MPa)	209.0
Martensite start temperature, M_s (K)	237.0
Martensite end temperature, M_f (K)	218.0
Austenite start temperature, A_s (K)	254.0
Austenite end temperature, A_f (K)	282.0
Reference temperature, T_{ref} (K)	320.0
σ vs. T slope (loading), $C_M\vert_{\sigma=300\mathrm{MPa}}$ (MPa/K)	5.5
σ vs. T slope (unloading), $C_A\vert_{\sigma=300\mathrm{MPa}}$ (MPa/K)	5.5
Material toughness G_c (kJ/m^2)	22.5

listed in Table 1 but conduct our numerical experiments at $T = 293$ K, and this is referred to as C3. The three stress-strain responses resulting from these material choices are shown in Figure 2B. It can be seen that C2 results in a smaller hysteresis loop, relative to the reference material (C1), and that the reduction in temperature of C3 results in lower stress transformation thresholds. The same fracture properties are assumed for all cases; namely, a toughness of $G_c = 22.5\,\mathrm{kJ/m^2}$, based on the data reported for NiTi,[63] and a length scale of $\ell = 0.145$ mm, which corresponds to a strength of 600 MPa according to Equation (3A). Symmetric tension-compression behavior is assumed but the focus will be on tensile behavior; case studies where the load ratio R is positive. As shown in Figure 3, two types of cyclic loading histories will be used. The first one, Figure 3A, is a sinusoidal loading history characterized by a maximum strain ε_{max}, a minimum strain ε_{min}, an initial strain amplitude ε_0, and a strain range $\Delta\varepsilon = \varepsilon_{max} - \varepsilon_{min}$. Considering also the definitions of load ratio $R = \varepsilon_{min}/\varepsilon_{max}$ and mean load ε_m, the sinusoidal loading history can be described as

$$\varepsilon = \varepsilon_m + \frac{\Delta\varepsilon}{2}\sin(f 2\pi t) = \frac{\Delta\varepsilon}{2} + R\frac{\Delta\varepsilon}{(1-R)} + \frac{\Delta\varepsilon}{2}\sin(f 2\pi t), \tag{28}$$

where f is the loading frequency and the strain amplitude is given by $\varepsilon_a = \varepsilon_{max} - \varepsilon_m$. Additionally, we will also consider a piece-wise linear variation of the applied displacement under constant amplitude, as shown in Figure 3B.

4.1 | Virtual $\Delta\varepsilon - N$ curves

We begin by conducting virtual uniaxial tests to estimate the load range versus number of cycles response, $\Delta\varepsilon - N$

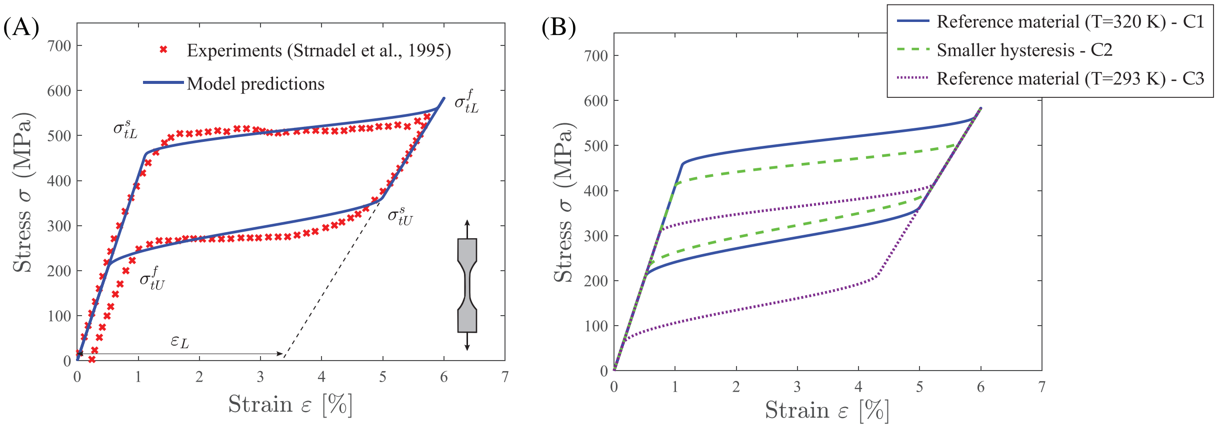

FIGURE 2 SMA constitutive behavior: (A) reference material (C1), obtained by calibrating with the experiments by Strandel et al.[62] on an equiatomic NiTi; (B) three choices of material behavior aimed at investigating the role of the stress-strain hysteresis (C2) and the temperature (C3) [Colour figure can be viewed at wileyonlinelibrary.com]

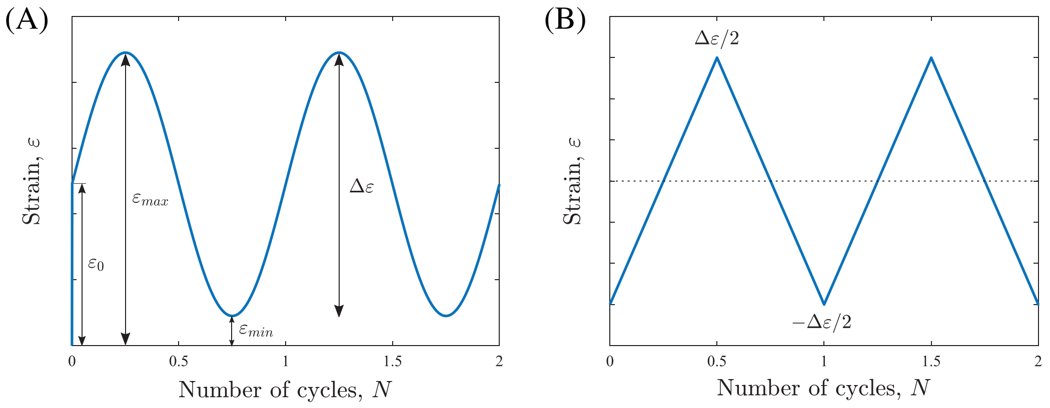

FIGURE 3 Cyclic loading histories employed: (A) sinusoidal, and (B) piece-wise linear, shown here for a loading frequency of 1 Hz [Colour figure can be viewed at wileyonlinelibrary.com]

curves. As shown in Figure 4, we mimic the one-dimensional conditions of uniaxial testing by using a single square element and defining a tensile strain range $\Delta\varepsilon$ by prescribing the vertical displacement of the top edge Δu^{∞}. The sinusoidal loading history shown in Figure 3A is used, with $R = 0.1$. Calculations are conducted using the phase field `AT2` model. The results obtained for the three material behaviors under consideration are shown in Figure 4, with each marker corresponding to one virtual tensile experiment.

In all three cases, the results reveal a significant increase in the fatigue life with decreasing loading range, up to the point of appearing to show an endurance limit. The profile displayed agrees with that exhibited by experimental $\Delta\varepsilon - N$ curves.[12] The three material behaviors considered exhibit a similar fatigue life for high loading ranges but differ significantly for low values of $\Delta\varepsilon$. For example, a strain range of $\Delta\varepsilon/\varepsilon_c = 0.4$ results in a fatigue life of 16,100 cycles for the reference material (C1), while the number of cycles to failure is only 3,533 and 1,761 for the cases of C2 and C3, respectively. These results can be justified by the lower stress (and strain) thresholds for phase transformations of C2 and C3 relative to C1—see Figure 2B. Inelastic transformation strains also accumulate in lower load levels and drive the evolution of fatigue damage. This is in agreement with experiments; samples that are initially in the austenitic phase exhibit shorter fatigue lives if the transformation stress is reduced.[12] It has been suggested that increasing the transformation stress threshold will lead to an improved fatigue performance.[16]

4.2 | Cracked square subjected to cyclic uniaxial loading

The second case study deals with a paradigmatic benchmark in phase field fracture: crack propagation in a square plate subjected to tension; see Figure 5A. As in previous studies,[25,26,32] we prescribe the remote load in a piece-wise linear manner. The material properties of Table 1 are adopted in this example; that is, we use C1, the reference material, and assume a test temperature of $T = 320\,\mathrm{K}$. The focus is on assessing the influence of the constitutive choice for the crack density function: `AT1` versus `AT2` models. The geometry, dimensions, and loading configuration are given in Figure 5A. An initial horizontal crack is introduced geometrically, which goes

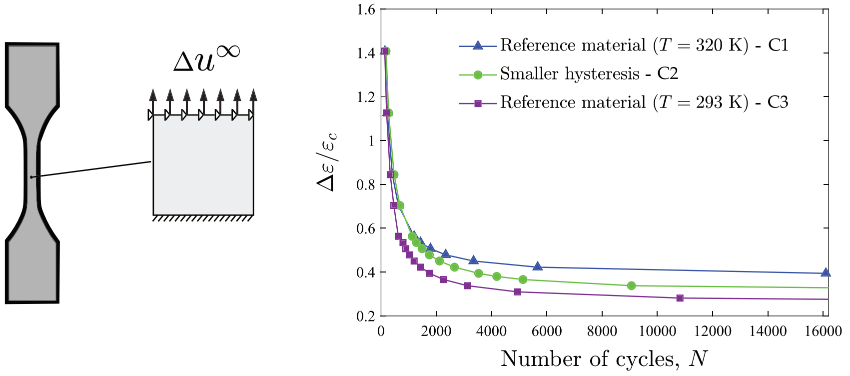

FIGURE 4 Virtual $\Delta\varepsilon - N$ curves for the three material behaviors considered. The strain range $\Delta\varepsilon$ is normalized by the critical strain, as given by Equation (3B) [Colour figure can be viewed at wileyonlinelibrary.com]

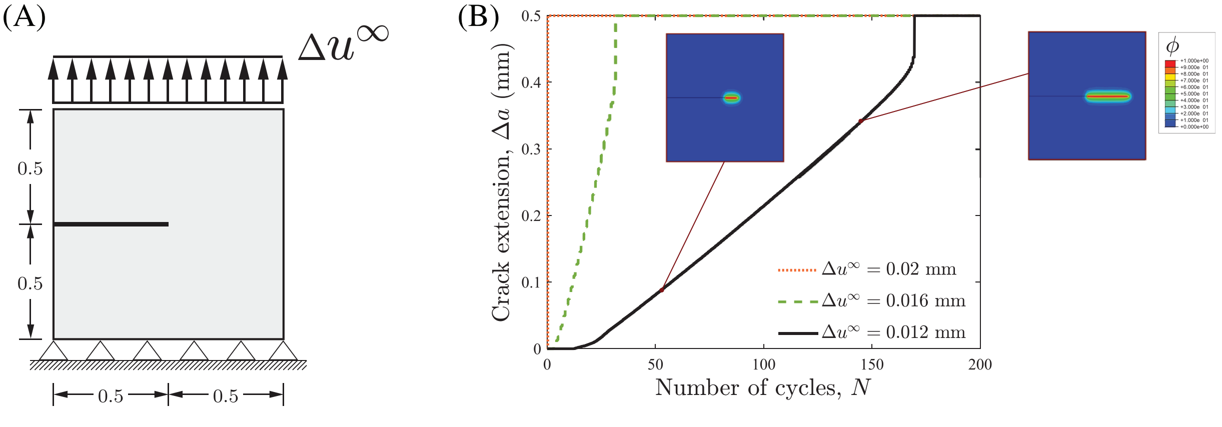

FIGURE 5 Cracked square plate: (A) dimensions (in mm) and loading configuration, and (B) crack extension versus number of cycles results for varying load ranges. The results have been obtained with the `AT1` model [Colour figure can be viewed at wileyonlinelibrary.com]

from the left side of the specimen to its center. The domain is discretized with approximately 23,000 linear quadrilateral elements, with the characteristic element length in the crack growth region being two orders of magnitude smaller than the phase field length scale, which is more than sufficient to ensure mesh convergence.[52,64] The results obtained for different load amplitudes and the `AT1` model are shown in Figure 5B. In agreement with expectations, we observe a faster crack growth rate with increasing Δu^{∞}. The crack propagates in a stable manner, following the expected mode I crack path, as in the case of static loading.[8]

We proceed to compare the predictions obtained with the `AT2` and `AT1` phase field models. The same magnitude of G_c and ℓ is assumed in both cases, which leads to different values of the critical stress and the critical strain - see Equations (2) and (3). As shown in Figure 6, the predictions obtained with both models show a rather close agreement but their ranking, in terms of fatigue life, is sensitive to the load range. First, for both $\Delta u^{\infty} = 0.016$ and 0.012 mm, we can observe that the initiation of crack growth takes place earlier for the `AT2` model. This is attributed to the presence of a damage threshold in the `AT1` model and to the higher material strength that is obtained for `AT1` if the same G_c and ℓ are sampled in Equations (2) and (3). A similar observation has been recently made in the context of fatigue crack growth in nonlinear kinematic and isotropic hardening elastic-plastic solids.[65] However, in both Figures 6A and 6B, fatigue crack growth rates appear to be larger for the `AT2` model, bringing predictions closer together, in the case of $\Delta u^{\infty} = 0.016$ mm and even resulting in a shorter fatigue life for the case of $\Delta u^{\infty} = 0.012$ mm. It should be noted that, for a given ℓ and G_c, the critical strain is larger for `AT1` relative to the `AT2` case - see Equations (2) and (3).

4.3 | Boundary layer model: Paris law behavior

Crack growth rates under small transformation zone conditions are quantified to assess the influence of testing temperature and hysteresis shape on the Paris law regime. Here, it should be emphasized that Paris law curves are an outcome of the model, a prediction and not an input. As outlined in Figure 7A, a boundary layer model is used, whereby a remote elastic K_I field is prescribed by defining the displacement of the nodes located in the outer boundary in agreement with William's[66] solution. Accordingly, the horizontal and vertical displacements in the outer nodes are, respectively, equal to

$$u_x = K_I \frac{1+\nu_A}{E_A}\sqrt{\frac{r}{2\pi}}(3-4\nu_A-\cos\theta)\cos\left(\frac{\theta}{2}\right), \tag{29}$$

$$u_y = K_I \frac{1+\nu_A}{E_A}\sqrt{\frac{r}{2\pi}}(3-4\nu_A-\cos\theta)\sin\left(\frac{\theta}{2}\right), \tag{30}$$

where r and θ are the coordinates of a polar coordinate system centered at the crack tip. For normalization purposes, a reference stress intensity factor can be defined as:

$$K_0 = \sqrt{\frac{E_A G_c}{(1-\nu_A^2)}}, \tag{31}$$

together with the following fracture process zone length:

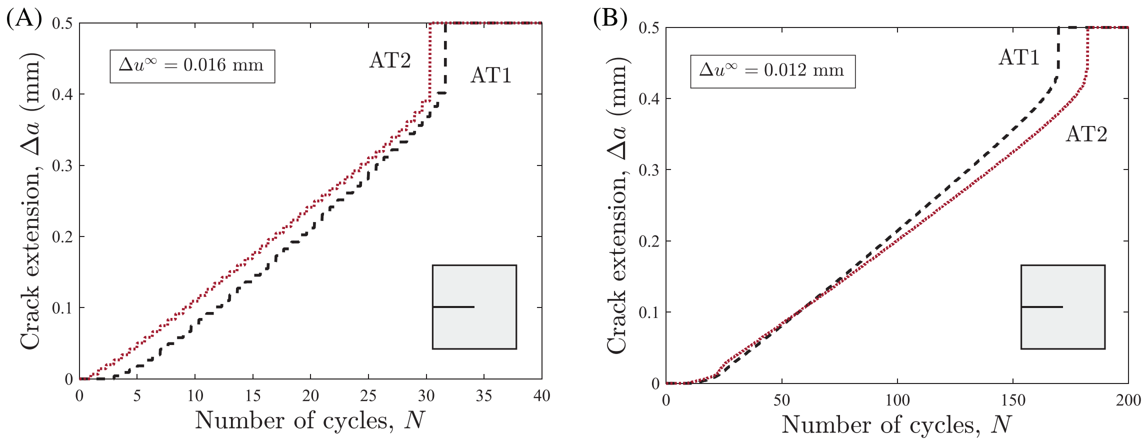

FIGURE 6 Cracked square plate. Influence of the constitutive choice for the crack density function, `AT1`[30] versus `AT2`[31] formulations: crack extension versus number of cycles for load ranges (A) $\Delta u^{\infty} = 0.016$ mm, and (B) $\Delta u^{\infty} = 0.012$ mm [Colour figure can be viewed at wileyonlinelibrary.com]

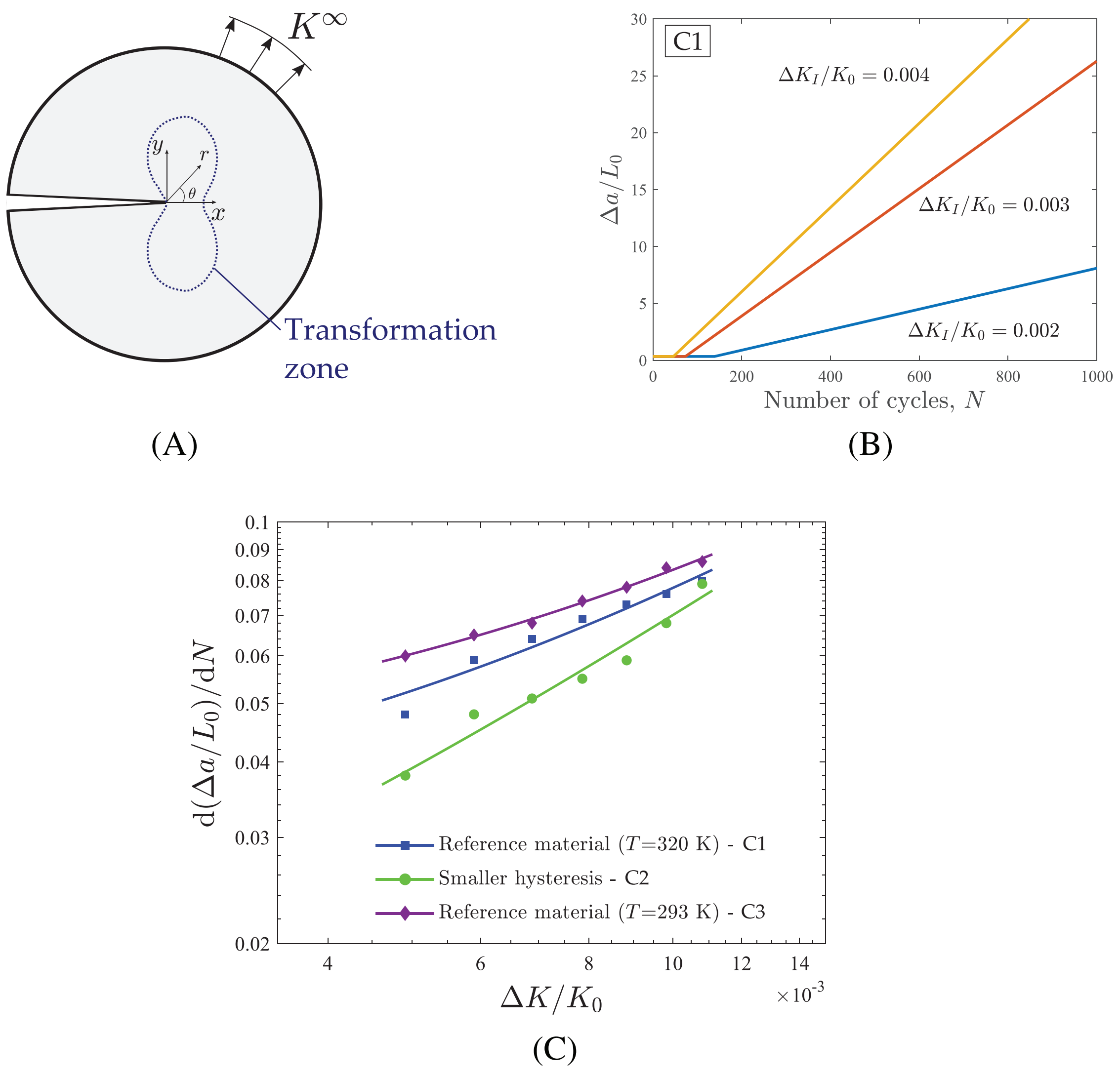

FIGURE 7 Boundary layer model, crack growth rates in the Paris law regime: (A) sketch of the boundary layer configuration and the small transformation zone assumption, (B) crack extension versus number of cycles for various loading ranges, and (C) fatigue crack growth rate versus load range for the three material behaviors considered [Colour figure can be viewed at wileyonlinelibrary.com]

$$L_0 = \frac{G_c\left(1-\nu_A^2\right)}{E_A}. \tag{32}$$

The model uses a total of 42,081 degrees-of-freedom (DOF), and the characteristic element length along the crack propagation region is taken to be more than 10 times smaller than the phase field length scale. The finite element results obtained for the three material behavior case studies considered are shown in Figure 7. First, curves of crack extension ($\Delta a/L_0$) versus number of cycles (N) are obtained for various loading amplitudes (Figure 7B). The slope of the curve is then measured and plotted against the load range ($\Delta K/K_0$) in a log–log plot (Figure 7C). It can be seen that, in agreement with expectations, the model predicts increasing fatigue crack growth rates with rising load amplitude.

The results obtained reveal several interesting patterns. First, differences are relatively small between the three cases. A fit to the well-known Paris law expression,

$$\frac{da}{dN} = C\Delta K^m, \tag{33}$$

gives values of m ranging from 1.2 to 1.4. A small influence of the martensitic transformation on Paris law parameters has also been observed experimentally, but slightly larger values have been reported for the Paris law coefficient m in NiTi; from $m = 2.2$ to $m = 3$, depending on the testing environment and alloy composition.[12,67,68] Second, faster crack growth rates are observed when decreasing the temperature, in agreement with the susceptibility trends observed for the uniaxial experiments

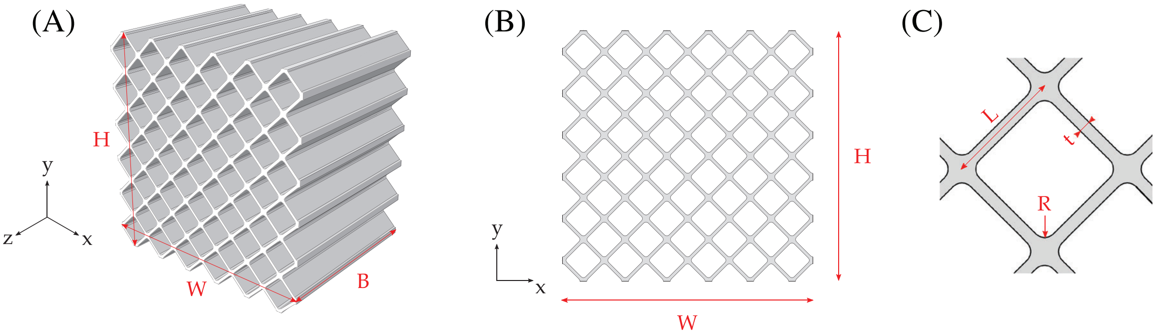

FIGURE 8 Geometry of the 3D lattice: (A) isometric view, (B) front view, and (C) details of the individual struts [Colour figure can be viewed at wileyonlinelibrary.com]

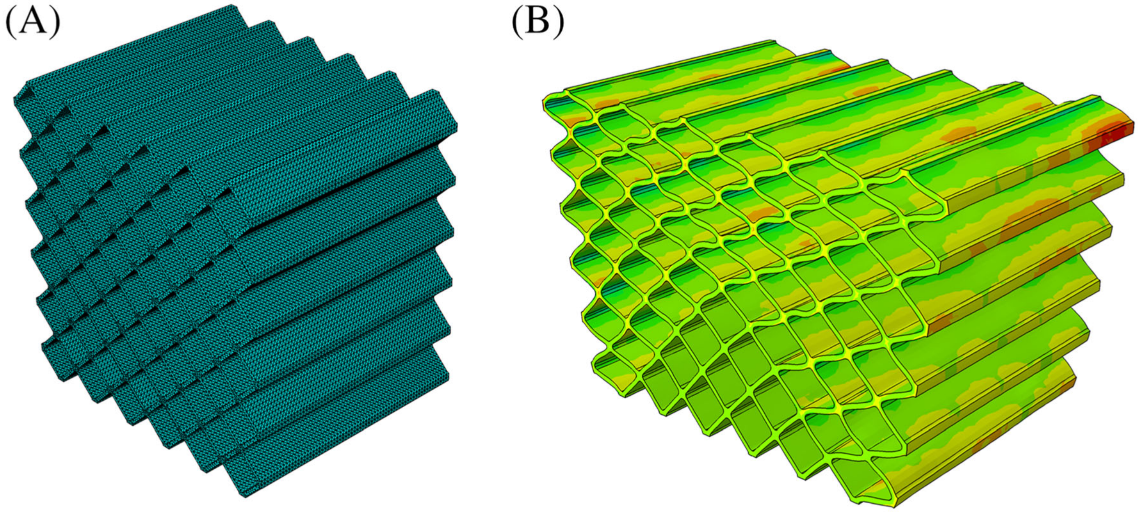

FIGURE 9 3D lattice: (A) finite element mesh, and (B) deformed shape at u_{min} with a scale factor of 10 [Colour figure can be viewed at wileyonlinelibrary.com]

(see Figure 4). This is also in agreement with experimental testing - the higher the temperature the higher the cycles to failure and the lower the crack growth rate.[68] Finally, the smaller hysteresis material (C2) exhibits lower crack growth rates, particularly for small ΔK values. This appears to contradict the results obtained under uniaxial tension, where the reference material exhibited the highest resistance to fatigue damage. Smaller hysteresis has been related to longer fatigue lives and thus is particularly suited for fast response actuators and precision control applications in the aerospace sector.[17]

4.4 | Fatigue failure of a 3D lattice

Finally, we demonstrate the capabilities of the modeling framework in predicting fatigue failures in complex geometries at large scales. In particular, we simulate the failure of a diamond lattice structure under repeated compression cycles.[69] The geometry of the diamond lattice material simulated is shown in Figure 8 through its isometric and in-plane views. The height and the width equal $H = W = 18$ mm, while the depth equals $B = 13$ mm. Each individual strut has a length of $L = 2.09$ mm and a thickness of $t = 0.2$ mm. A filet radius of $R = 0.2$ mm is introduced to suppress stress singularities.

The entire geometry is modeled to showcase the efficiency of the computational framework in dealing with large scale problems. The domain is discretized with 10-node quadratic tetrahedral elements. As shown in Figure 9A, the mesh is uniform and the characteristic element length equals 0.2 mm, which is 5 times smaller than the phase field length, which is taken to be equal to $\ell = 1$ mm in this case study. All the other properties are those listed in Table 1 (the reference material), and the phase field `AT2` model is used. The model contains more

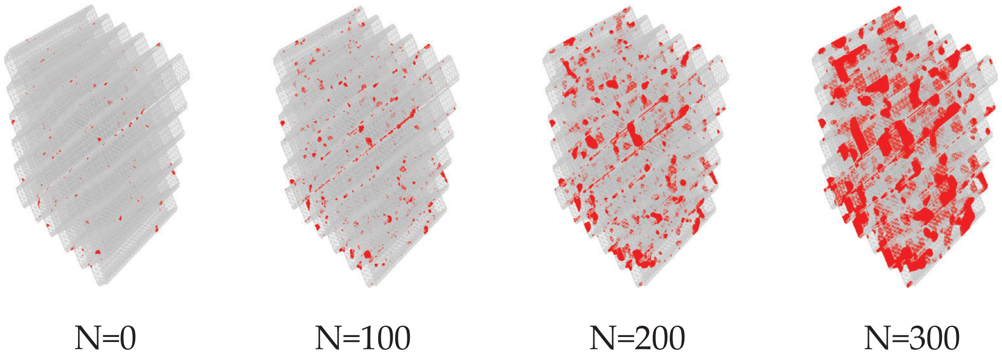

FIGURE 10 3D lattice. Contours of defects (regions with $\phi > 0.95$) as a function of the number of loading cycles. Results are shown in the undeformed state [Colour figure can be viewed at wileyonlinelibrary.com]

than 7 million DOFs and is run in parallel, using 16 cores. The diamond lattice has its three displacement components constrained at the bottom ($y = 0$) and is subjected to a vertical (u_y) displacement at the top. The cyclic load is applied using a piece-wise linear amplitude (Figure 3B), with a load range of 0.2 mm, with $u_{max} = 0$ and $u_{min} = -0.2$ mm. The deformed shape of the lattice undergoing compression is shown in Figure 9B, upon the application of a scaling factor of 10. It can be observed that, as expected, the struts located near the center of the top side of the lattice undergo the largest deformations.

An initial distribution of defects is randomly assigned to account for the role that initial cracks and voids can play in the fatigue failure process. This is particularly relevant for these lattice structures as they are typically fabricated using additive manufacturing. The initial distribution of defects is shown in Figure 10A, where the areas with $\phi > 0.95$ have been plotted before applying mechanical load. Figure 10B–D shows the evolution of defects in time. It can be observed that the initial defects grow and eventually merge with neighboring defects, leading to the nucleation of cracks of significant size and the loss of load carrying capacity. The capabilities of the present computational framework in capturing complex cracking phenomena are demonstrated.

5 | CONCLUSIONS

We have presented a new formulation for predicting fatigue crack growth in SMAs. The model is based on a phase field description of the crack-solid interface and accommodates the two main constitutive choices for the crack density function, the so-called `AT1` and `AT2` approaches. This phase field description has been enriched with a fatigue degradation function and a fatigue history variable. Damage, static and cyclic, is driven by the total strain energy density, including contributions from both elastic and transformation mechanical fields. Material deformation is captured by the constitutive model for SMAs developed by Auricchio and Taylor,[29] where a Drucker–Prager type of transformation surface is used. The theoretical framework is numerically implemented using the finite element method, and a robust monolithic quasi-Newton solution scheme is used to significantly reduce the computational cost. The computational model is used to simulate fatigue failures in multiple configurations. Several loading histories, sinusoidal and piece-wise linear, are adopted. Three case studies are considered for the material parameters with the aim of gaining insight into the role of transformation stress thresholds, temperature, and shape of the hysteresis zone. Our simulations address: (i) the $\Delta\varepsilon$ versus number of cycles to failure response of smooth samples undergoing uniaxial tension, (ii) the growth of fatigue cracks in single edge notched specimens, (iii) the prediction of fatigue crack growth rates to quantify Paris law parameters, and (iv) the fatigue failure of a 3D diamond lattice structure. The results are mechanistically interpreted and discussed in the context of the experimental fatigue SMA literature. The main findings are as follows:

- The model adequately captures the fatigue behavior of SMAs, including the sensitivity to temperature and to the stress-strain hysteresis size of fatigue crack growth rates and the number of cycles to failure.
- The comparison between `AT1` and `AT2` phase field models reveals that the initiation of growth occurs first for `AT2` but that higher fatigue crack growth rates are predicted by the `AT1` formulation.
- The phase transformation process has a limited effect on Paris law coefficients, in agreement with experimental observations. However, the m values attained are slightly below those measured in the literature.

- Complex fatigue cracking phenomena can be captured efficiently and without convergence problems. These include the growth and coalescence of multiple defects in arbitrary geometries and dimensions.

The framework developed can be used to optimize the design of SMA components and map safe regimes of operation. Potential avenues for future work include the modeling of thermal fatigue and extending the model to account for plasticity.

ACKNOWLEDGMENTS

M. Simoes acknowledges financial support from the Engineering and Physical Sciences Research Council (grant EP/R512461/1) and from the European Space Agency (Contract no. 4000125861). E. Martínez-Pañeda was supported by an UK Research and Innovation Future Leaders Fellowship (grant MR/V024124/1).

CONFLICT OF INTEREST

The authors declare that they have no conflicts of interest.

AUTHOR CONTRIBUTIONS

Marlini Simoes performed the conceptualization, data curation, formal analysis, investigation, methodology, software, validation, visualization, and writing—original draft preparation. Cristopher Braithwaite did the funding acquisition, project administration, supervision, and writing—review and editing. Advenit Makaya did the funding acquisition, project administration, and supervision. Emilio Martínez-Pañeda performed the conceptualization, data curation, formal analysis, investigation, methodology, project administration, resources, software, supervision, visualization, and writing—review and editing.

DATA AVAILABILITY STATEMENT

The data generated during this study will be made available upon reasonable request. The data that support the findings of this study are available from the corresponding author upon reasonable request.

ORCID

Marlini Simoes https://orcid.org/0000-0002-2237-3276
Emilio Martínez-Pañeda https://orcid.org/0000-0002-1562-097X

REFERENCES

1. Lagoudas DC. *Shape Memory Alloys: Modeling and Engineering Applications*. Berlin: Springer; 2008.
2. Hartl DJ, Lagoudas DC. Aerospace applications of shape memory alloys. *Proc Inst Mech Eng Part G: J Aerosp Eng*. 2007;221(4):535-552.
3. Robertson SW, Ritchie RO. In vitro fatigue-crack growth and fracture toughness behavior of thin-walled superelastic Nitinol tube for endovascular stents: a basis for defining the effect of crack-like defects. *Biomaterials*. 2007;28(4):700-709.
4. Baxevanis T, Lagoudas DC. Fracture mechanics of shape memory alloys: review and perspectives. *Int J Fract*. 2015;191(1-2):191-213.
5. Baxevanis T, Parrinello AF, Lagoudas DC. On the fracture toughness enhancement due to stress-induced phase transformation in shape memory alloys. *Int J Plast*. 2013;50:158-169.
6. Gollerthan S, Young ML, Neuking K, Ramamurty U, Eggeler G. Direct physical evidence for the back-transformation of stress-induced martensite in the vicinity of cracks in pseudoelastic NiTi shape memory alloys. *Acta Mater*. 2009;57(19):5892-5897.
7. Freed Y, Banks-Sills L. Crack growth resistance of shape memory alloys by means of a cohesive zone model. *J Mech Phys Solids*. 2007;55(10):2157-2180.
8. Simoes M, Martínez-Pañeda E. Phase field modelling of fracture and fatigue in Shape Memory Alloys. *Comput Methods Appl Mech Eng*. 2021;373:113504.
9. Maletta C, Sgambitterra E, Furgiuele F. Crack tip stress distribution and stress intensity factor in shape memory alloys. *Fatigue Fract Eng Mater Struct*. 2013;36(9):903-912.
10. Baxevanis T, Landis CM, Lagoudas DC. On the fracture toughness of pseudoelastic shape memory alloys. *J Appl Mech Trans ASME*. 2014;81(4):1-8.
11. Haghgouyan B, Hayrettin C, Baxevanis T, Karaman I, Lagoudas DC. Fracture toughness of NiTi-Towards establishing standard test methods for phase transforming materials. *Acta Mater*. 2019;162:226-238.
12. Wilkes KE, Liaw PK. Fatigue behavior of shape-memory alloys. *JOM*. 2000;52(10):45-51.
13. Eggeler G, Hornbogen E, Yawny A, Heckmann A, Wagner M. Structural and functional fatigue of NiTi shape memory alloys. *Mater Sci Eng A*. 2004;378(1-2 SPEC. ISS.):24-33.
14. Ghafoori E, Hosseini E, Leinenbach C, Michels J, Motavalli M. Fatigue behavior of a Fe-Mn-Si shape memory alloy used for prestressed strengthening. *Mater Des*. 2017;133:349-362.
15. Hornbogen E. Some effects of martensitic transformation on fatigue resistance. *Fatigue Fract Eng Mater Struct*. 2002;25(8-9):785-790.
16. Hornbogen E. Thermo-mechanical fatigue of shape memory alloys. *J Mater Sci*. 2004;39(2):385-399.
17. Lagoudas DC, Miller DA, Rong L, Kumar PK. Thermomechanical fatigue of shape memory alloys. *Smart Mater Struct*. 2009;18:8.
18. Robertson SW, Pelton AR, Ritchie RO. Mechanical fatigue and fracture of Nitinol. *Int Mater Rev*. 2012;57(1):1-36.
19. Hashemi YM, Kadkhodaei M, Mohammadzadeh MR. Fatigue analysis of shape memory alloy helical springs. *Int J Mech Sci*. 2019;161-162:105059.
20. Wang J, Zhang W, Zhu J, Xu Y, Gu X, Moumni Z. Finite element simulation of thermomechanical training on functional stability of shape memory alloy wave spring actuator. *J Intell Mater Syst Struct*. 2019;30(8):1239-1251.
21. Xiao Y, Jiang D. Constitutive modelling of transformation pattern in superelastic NiTi shape memory alloy under cyclic loading. *Int J Mech Sci*. 2020;105743:182.

22. Wang GZ. A finite element analysis of evolution of stress-strain and martensite transformation in front of a notch in shape memory alloy NiTi. *Mater Sci Eng A*. 2007;460-461:383-391.
23. Wang GZ, Xuan FZ, Tu ST, Wang ZD. Effects of triaxial stress on martensite transformation, stress-strain and failure behavior in front of crack tips in shape memory alloy NiTi. *Mater Sci Eng A*. 2010;527(6):1529-1536.
24. Lagoudas DC, Bo Z, Qidwai MA. A unified thermodynamic constitutive model for SMA and finite element analysis of active metal matrix composites. *Mech Compos Mater Struct*. 1996;3(2):153-179.
25. Carrara P, Ambati M, Alessi R, De Lorenzis L. A framework to model the fatigue behavior of brittle materials based on a variational phase-field approach. *Comput Methods Appl Mech Eng*. 2731;361(11):2020.
26. Golahmar A, Kristensen PK, Niordson CF, Martínez-Pañeda E. A phase field model for hydrogen-assisted fatigue. *Int J Fatigue*. 2022;154:106521.
27. Navidtehrani Y, Betegón C, Martínez-Pañeda E. A unified Abaqus implementation of the phase field fracture method using only a user material subroutine. *Materials*. 2021;14(8):1913.
28. Wu J-Y, Nguyen VP, Nguyen CT, Sutula D, Sinaie S, Bordas S. Phase-field modelling of fracture. *Adv Appl Mech*. 2020;53:1-183.
29. Auricchio F, Taylor RL. Shape-memory alloys: modelling and numerical simulations of the finite-strain superelastic behavior. *Comput Methods Appl Mech Eng*. 1997;143(96):175-194.
30. Pham K, Amor H, Marigo JJ, Maurini C. Gradient damage models and their use to approximate brittle fracture. *Int J Damage Mech*. 2011;20(4):618-652.
31. Bourdin B, Francfort GA, Marigo J-J. Numerical experiments in revisited brittle fracture. *J Mech Phys Solids*. 2000;48(4):797-826.
32. Kristensen PK, Martínez-Pañeda E. Phase field fracture modelling using quasi-Newton methods and a new adaptive step scheme. *Theor Appl Fract Mech*. 2446;107(10):2020.
33. Wu J-Y, Huang Y, Nguyen VP. On the BFGS monolithic algorithm for the unified phase field damage theory. *Comput Methods Appl Mech Eng*. 2704;360(11):2020.
34. Provatas N, Elder K. *Phase-Field Methods in Materials Science and Engineering*. Weinheim, Germany: John Wiley & Sons; 2011.
35. Cui C, Ma R, Martínez-Pañeda E. A phase field formulation for dissolution-driven stress corrosion cracking. *J Mech Phys Solids*. 2021;147:104254.
36. Borden MJ, Verhoosel CV, Scott MA, Hughes TJR, Landis CM. A phase-field description of dynamic brittle fracture. *Comput Methods Appl Mech Eng*. 2012;217-220:77-95.
37. Kristensen PK, Niordson CF, Martínez-Pañeda E. Applications of phase field fracture in modelling hydrogen assisted failures. *Theor Appl Fract Mech*. 2837;110(10):2020.
38. Peng F, Huang W, Ma Y, Zhang ZQ, Fu N. Fourth-order phase field model with spectral decomposition for simulating fracture in hyperelastic material. *Fatigue Fract Eng Mater Struct*. 2021;44(9):2372-2388.
39. Zhou X, Jia Z, Berto F. Simulation of cracking behaviours in interlayered rocks with flaws subjected to tension using a phase-field method. *Fatigue Fract Eng Mater Struct*. 2019;42(8):1679-1698.
40. Hirshikesh, Natarajan S, Annabattula RK, Martínez-Pañeda E. Phase field modelling of crack propagation in functionally graded materials. *Compos Part B Eng*. 2019;169:239-248.
41. Kumar PKAV, Dean A, Reinoso J, Lenarda P, Paggi M. Phase field modeling of fracture in Functionally Graded Materials: G -convergence and mechanical insight on the effect of grading. *Thin-Walled Struct*. 2021;107234:159.
42. Bui TQ, Hu X. A review of phase-field models, fundamentals and their applications to composite laminates. *Eng Fract Mech*. 2021;248:107705.
43. Quintanas-Corominas A, Reinoso J, Casoni E, Turon A, Mayugo JA. A phase field approach to simulate intralaminar and translaminar fracture in long fiber composite materials. *Compos Struct*. 2019;220:899-911.
44. Tan W, Martínez-Pañeda E. Phase field predictions of microscopic fracture and R-curve behaviour of fibre-reinforced composites. *Compos Sci Technol*. 2021;202:108539.
45. Aldakheel F, Noii N, Wick T, Wriggers P. A global-local approach for hydraulic phase-field fracture in poroelastic media. *Comput Math Appl*. 2021;91:99-121.
46. Zhou S, Zhuang X, Zhu H, Rabczuk T. Phase field modelling of crack propagation, branching and coalescence in rocks. *Theor Appl Fract Mech*. 2018;96:174-192.
47. Alessi R, Ambati M, Gerasimov T, Vidoli S, De Lorenzis L. Comparison of phase-field models of fracture coupled with plasticity. In: MCE Oñate, D Peric, E de Souza- Neto, eds. *Advances in Computational Plasticity*: Springer Nature; 2018:1-21.
48. Borden MJ, Hughes TJR, Landis CM, Anvari A, Lee IJ. A phase-field formulation for fracture in ductile materials: finite deformation balance law derivation, plastic degradation, stress triaxiality effects. *Comput Methods Appl Mech Eng*. 2016;312:130-166.
49. Shishvan SS, Assadpour-asl S, Martínez-Pañeda E. A mechanism-based gradient damage model for metallic fracture. *Eng Fract Mech*. 2021;255:107927.
50. Anand L, Mao Y, Talamini B. On modeling fracture of ferritic steels due to hydrogen embrittlement. *J Mech Phys Solids*. 2019;122:280-314.
51. Kristensen PK, Niordson CF, Martínez-Pañeda E. A phase field model for elastic-gradient-plastic solids undergoing hydrogen embrittlement. *J Mech Phys Solids*. 2020;143:104093.
52. Martínez-Pañeda E, Golahmar A, Niordson CF. A phase field formulation for hydrogen assisted cracking. *Comput Methods Appl Mech Eng*. 2018;342:742-761.
53. Mandal TK, Gupta A, Nguyen VP, Chowdhury R, de Vaucorbeil A. A length scale insensitive phase field model for brittle fracture of hyperelastic solids. *Eng Fract Mech*. 2020;236(June):107196.
54. Yin S, Yang W, Kwon J, Wat A, Meyers MA, Ritchie RO. Hyperelastic phase-field fracture mechanics modeling of the toughening induced by Bouligand structures in natural materials. *J Mech Phys Solids*. 2019;131:204-220.
55. Griffith AA. The phenomena of rupture and flow in solids. *Phil Trans A*. 1920;221:163-198.
56. Bourdin B, Francfort GA, Marigo JJ. *The Variational Approach to Fracture*. Netherlands: Springer; 2008.
57. Kristensen PK, Niordson CF, Martínez-Pañeda E. An assessment of phase field fracture: crack initiation and growth. *Phil Trans R Soc A: Math Phys Eng Sci*. 2021;379:20210021.

58. Tanné E, Li T, Bourdin B, Marigo J-J, Maurini C. Crack nucleation in variational phase-field models of brittle fracture. *J Mech Phys Solids*. 2018;110:80-99.
59. Auricchio F, Taylor RL, Lubliner J. Shape-memory alloys: macromodelling and numerical simulations of the superelastic behavior. *Comput Methods Appl Mech Eng*. 1997;146(96): 281-312.
60. Matthies H, Strang G. The solution of nonlinear finite element equations. *Int J Numer Methods Eng*. 1979;14:1613-1626.
61. Papazafeiropoulos G, Muñiz-Calvente M, Martínez-Pañeda E. Abaqus2Matlab: a suitable tool for finite element post-processing. *Adv Eng Softw*. 2017;105:9-16.
62. Strnadel B, Ohashi S, Ohtsuka H, Miyazaki S, Ishihara T. Effect of mechanical cycling on the pseudoelasticity characteristics of TiNi and TiNiCu alloys. *Mater Sci Eng A*. 1995;203(1-2): 187-196.
63. Haghgouyan B, Hayrettin C, Baxevanis T, Karamanm I, Lagoudas DC. On the experimental evaluation of the fracture toughness of shape memory alloys. *In TMS Annual Meeting & Exhibition*: Springer; 2018:565-573.
64. Pandolfi A, Weinberg K, Ortiz M. A comparative accuracy and convergence study of eigenerosion and phase-field models of fracture. *Comput Methods Appl Mech Eng*. 2021;386:114078.
65. Khalil Z, Elghazouli AY, Martínez-Pañeda E. A generalised phase field model for fatigue crack growth in elastic - plastic solids with an efficient monolithic solver. *Comput Methods Appl Mech Eng*. 2022;388:114286.
66. Williams ML. On the stress distribution at the base of a stationary crack. *J Appl Mech*. 1957;24:109-114.
67. Haghgouyan B, Young B, Picak S, Baxevanis T, Karaman I, Lagoudas DC. A unified description of mechanical and actuation fatigue crack growth in shape memory alloys. *Acta Mater*. 2021;117155:217.
68. Sgambitterra E, Maletta C, Magarò P, Renzo D, Furgiuele F, Sehitoglu H. Effects of temperature on fatigue crack propagation in pseudoelastic NiTi shape memory alloys. *Shape Memory Superelasticity*. 2019;5(3):278-291.
69. Côté F, Deshpande VS, Fleck NA, Evans AG. The compressive and shear responses of corrugated and diamond lattice materials. *Int J Solids Struct*. 2006;43(20):6220-6242.

How to cite this article: Simoes M, Braithwaite C, Makaya A, Martínez-Pañeda E. Modelling fatigue crack growth in shape memory alloys. *Fatigue Fract Eng Mater Struct*. 2022;45(4): 1243-1257. doi:10.1111/ffe.13638